Synergy between inhibitors of two mitotic spindle assembly motors undermines an adaptive response

April L. Solon[a], Taylor M. Zaniewski[b], Patrick O'Brien[c], Martin Clasby[c], William O. Hancock[d], and Ryoma Ohi[a,*]

[a]Department of Cell and Developmental Biology and [c]Vahlteich Medicinal Chemistry Core, University of Michigan, Ann Arbor, MI 48109; [b]Department of Chemistry and [d]Department of Biomedical Engineering, Pennsylvania State University, University Park, PA 16802

ABSTRACT **Mitosis is the cellular process that ensures accurate segregation of the cell's genetic material into two daughter cells. Mitosis is often deregulated in cancer; thus drugs that target mitosis-specific proteins represent attractive targets for anticancer therapy. Numerous inhibitors have been developed against kinesin-5 Eg5, a kinesin essential for bipolar spindle assembly. Unfortunately, Eg5 inhibitors (K5Is) have been largely ineffective in the clinic, possibly due to the activity of a second kinesin, KIF15, that can suppress the cytotoxic effect of K5Is by driving spindle assembly through an Eg5-independent pathway. We hypothesized that pairing of K5Is with small molecule inhibitors of KIF15 will be more cytotoxic than either inhibitor alone. Here we present the results of a high-throughput screen from which we identified two inhibitors that inhibit the motor activity of KIF15 both in vitro and in cells. These inhibitors selectively inhibit KIF15 over other molecular motors and differentially affect the ability of KIF15 to bind microtubules. Finally, we find that chemical inhibition of KIF15 reduces the ability of cells to acquire resistance to K5Is, highlighting the centrality of KIF15 to K5I resistance and the value of these inhibitors as tools with which to study KIF15 in a physiological context.**

Monitoring Editor
Claire Walczak
Indiana University

Received: Jun 27, 2022
Revised: Sep 20, 2022
Accepted: Sep 26, 2022

INTRODUCTION

Mitosis is the process by which chromosomes are segregated into two daughter cells. The complexity of cytoskeletal organization and dynamics and signaling pathways that orchestrate mitosis make it challenging to understand its molecular underpinnings and biophysical basis. Successful completion of mitosis requires that the chromosome segregation machinery, i.e., the mitotic spindle, has a bipolar geometry to accurately divide the genome. In most organisms, bipolarity of the mitotic spindle is generated by the mitotic kinesin, Kif11/Eg5 (Eg5) (Mann and Wadsworth, 2019), and its activity is counteracted by cytoplasmic dynein. However, it is clear that other motors can substitute for Eg5 and dynein. Simultaneous inhibition of both Eg5 and dynein leads to the formation of a bipolar spindle that can segregate chromosomes, albeit with reduced fidelity (Mitchison *et al.*, 2005). In this case, two additional mitotic kinesins—KIF15 and KifC1/HSET—substitute for Eg5 and dynein, respectively (Mountain *et al.*, 1999; Tanenbaum *et al.*, 2009; Vanneste *et al.*, 2009; Hentrich and Surrey, 2010). Moreover, motors and other microtubule-associated proteins link spindle microtubules in ways that are poorly understood, creating a network of interactions that collectively define systems-level properties of the mitotic spindle (Oriola *et al.*, 2018). These aspects of mitosis prevent conventional approaches such as RNA interference or gene deletion from painting a complete picture of mitotic mechanisms and underscore the importance of orthogonal approaches, for example, laser microsurgery (Maiato *et al.*, 2004) and small molecules (Kapoor *et al.*, 2000) in the study of mitosis. From the perspective of human health, the complexity of mitosis has made it a challenging process to target in the context of cancer.

This article was published online ahead of print in MBoC in Press (http://www.molbiolcell.org/cgi/doi/10.1091/mbc.E22-06-0225) on October 6, 2022.

*Address correspondence to: Ryoma Ohi (oryoma@umich.edu).

Abbreviations used: ATP, adenosine triphosphate; CRC, concentration response curve; DMEM, Dulbecco's Modified Eagle Medium; DMF, dimethylformamide; DMSO, dimethyl sulfoxide; K5I, kinesin-5 inhibitor; KIRC, kinesin-5 inhibitor resistant; STLC, S-trityl-L-cysteine; TFA, trifluoroacetic acid; THF, tetrahydrofuran.

The importance of Eg5 during spindle assembly has made it a major target for antimitotic drugs. Eg5, a member of the kinesin-5 family, is a homotetrameric plus-end-directed motor that participates in spindle assembly by sliding antiparallel microtubules apart (Kashina *et al.*, 1996; Kapitein *et al.*, 2005). The archetypal kinesin-5 inhibitor (K5I) monastrol blocks centrosome separation, yielding a preponderance of monopolar spindles(Mayer *et al.*, 1999). Studies with monastrol and other K5Is have uncovered fundamental knowledge of mitosis including the correction of flawed kinetochore–microtubule attachments (Khodjakov *et al.*, 2003; Lampson *et al.*, 2004), the basis of spindle bipolarity maintenance in mammalian cells (Kapoor *et al.*, 2000), and the discovery that KIF15 can substitute for Eg5 during spindle assembly (Tanenbaum *et al.*, 2009; Vanneste *et al.*, 2009). To date, more than 50 K5Is have been developed and many of them have been subjected to both preclinical studies and clinical trials. Although K5Is induce apoptosis of cultured cells as a result of failed mitoses (Kapoor *et al.*, 2000), K5Is have performed poorly in Phase I and II clinical trials, failing to induce tumor regression (Marzo and Naval, 2013). Several hypotheses have been posed to explain this disparity in results, including problems with drug uptake or efflux (Gampa *et al.*, 2020), dosing schedules that were too infrequent to effectively treat the tumors (Komlodi-Pasztor *et al.*, 2011), or the ability of cells to use an alternative spindle assembly pathway that depends on KIF15 (Tanenbaum *et al.*, 2009).

An ability of mammalian cells to switch to a KIF15-dependent spindle assembly pathway in the absence of Eg5 function is supported by several lines of evidence. Tanenbaum *et al.* showed that overexpression of the mitotic kinesin KIF15 restores bipolar spindle assembly in Eg5-inhibited or -depleted cells (Tanenbaum *et al.*, 2009). In addition, we and others showed that cells can accumulate genetic changes that allow KIF15 to substitute for Eg5 in spindle assembly when cultured in the presence of K5Is. Known changes that drive resistance to K5Is include 1) mutation of Eg5 itself (Kasap *et al.*, 2014), 2) overexpression of KIF15 (Tanenbaum *et al.*, 2009; Sturgill and Ohi, 2013), and 3) mutations in protein factors that allow KIF15 to bind the spindle more efficiently (Raaijmakers *et al.*, 2012; Sturgill *et al.*, 2016). In addition, EGF can drive the KIF15 pathway by weakening centrosome cohesion (Mardin *et al.*, 2013). The central role of KIF15 in mediating these resistance pathways suggests that KIF15 is essential for cells to acquire resistance to K5Is. Indeed, removal of KIF15 via CRISPR-Cas9 technology completely abrogates K5I resistance in HeLa cells, an effect that can be rescued by overexpression of exogenous KIF15 (Sturgill *et al.*, 2016). This provides evidence that KIF15 is both sufficient and necessary for spindle assembly in the absence of functional Eg5, which in turn rationalizes the use of KIF15 inhibitors as a chemotherapeutic agent that improves the performance of K5Is.

Currently, the field lacks a well-characterized selective chemical inhibitor of KIF15 with which to test this hypothesis. We previously described a pipeline to screen for KIF15 inhibitors and used this platform to identify GW108X, an oxindole that inhibits multiple kinases as well as KIF15 (Dumas *et al.*, 2019). Although GW108X has already proven useful to investigate kinetochore–microtubule organization in the mitotic spindle (Begley *et al.*, 2021), we continued our efforts to identify new KIF15 inhibitor scaffolds by high-throughput screening. Here we report two new KIF15 inhibitors, Munesib-1 and Fift-IN. We show that these molecules selectively block KIF15 activity both in vitro and in cells that rely on KIF15 to progress through mitosis. Similar to GW108X, our new inhibitors work via an allosteric mechanism rather than by targeting the ATP-binding pocket, but they offer the advantage that they do not suffer from off-target effects that we observe with GW1086, which presumably stem from its antikinase activity (Elkins *et al.*, 2016). Last, we show that Fift-IN synergizes with a K5I to reduce the occurrence of K5I resistance. Collectively, Munesib-1 and Fift-IN represent valuable tools for the scientific community with which to assay spindle mechanics in real time.

RESULTS

Identification of two potent KIF15 inhibitors via high-throughput screening

To identify new small molecule inhibitors of KIF15, we screened the Maybridge 24K Library of Small Molecule Inhibitors, a collection containing chemically diverse small molecule compounds, using a pipeline we described previously (Dumas *et al.*, 2019). In brief, this assay uses a luciferase reaction to couple ATPase activity to luminescence that is quantifiable by a plate reader (Figure 1A). We used KIF15-N420, a minimal dimer construct that exhibits microtubule-stimulated ATPase activity (Supplemental Figure S1, A and B), as the ATPase and taxol-stabilized microtubules as the substrate. In this assay, exclusion of ATP provides an idealized upper limit of 100% inhibition that would result from exposure to a perfect inhibitor. For a negative control, we included ATP but no compounds or microtubules, a condition that yields the baseline ATPase activity of uninhibited motor.

Before screening, we ran several initial tests to determine the robustness of our assay. First, we determined that the final luminescence signal was adequately stable over 60 min (Supplemental Figure S1C). Next, we varied the concentration of motor used in the assay (Supplemental Figure S1D). Higher concentrations of KIF15 produced higher luminescence and greater separation between the readouts of the positive and negative controls. Thus we chose to use a high concentration of enzyme (100 nM) for screening. Additionally, we tested our previously identified KIF15 inhibitor, GW108X (Dumas *et al.*, 2019), in this assay (Supplemental Figure S1D). As expected, addition of 20 μM GW108X to 100 nM KIF15 resulted in a 41% decrease in luminescence compared with the control, validating our assay. Last, we calculated the Z′ value of the assay, a statistical measure used to quantify the robustness of an assay. By running roughly 200 samples each of positive and negative controls, we determined the Z′ value to be 0.71 (Supplemental Figure S1E); as a Z′ between 0.5 and 1 indicates strong assay conditions, a Z′ of 0.71 verified that our assay is suitable for identifying KIF15 inhibitors.

In the first round of screening, we queried 23,552 compounds from the Maybridge 24K library (Figure 1B). As our positive control GW108X showed roughly 40% inhibition in this assay (Supplemental Figure S1D), we set the threshold above which to define "hits" at a conservative 20% inhibition of KIF15's ATPase activity, indicated by the red bar in Figure 1B. The average Z′ value for the assay plates was 0.82, indicating that our screening data were reliable; 1330 compounds showed 20% or greater inhibition of KIF15 and were then rescreened in triplicate in a "confirmation screen" (Figure 1C). Of 1330 compounds retested, 864 confirmed an average percent inhibition of greater or equal to 20%.

Compounds that passed the confirmation screen were then subjected to a "counterscreen" wherein they were tested against a different ATPase using the same ADP-Glo assay (Figure 1D). We selected hexokinase, an enzyme that phosphorylates six-sugar carbons in the first step of glycolysis (Wilson, 2003), as a nonspecific ATPase due to its highly distinct structure and function compared with KIF15. Our selection of a kinase for the counterscreen is due to our finding that the oxindole GW108X potently inhibits both KIF15 and a broad spectrum of kinases (Elkins *et al.*, 2016; Dumas *et al.*, 2019). Indeed, we sought to eliminate any promiscuous compounds that have nonspecific activity against ATPases; thus we set the criteria for

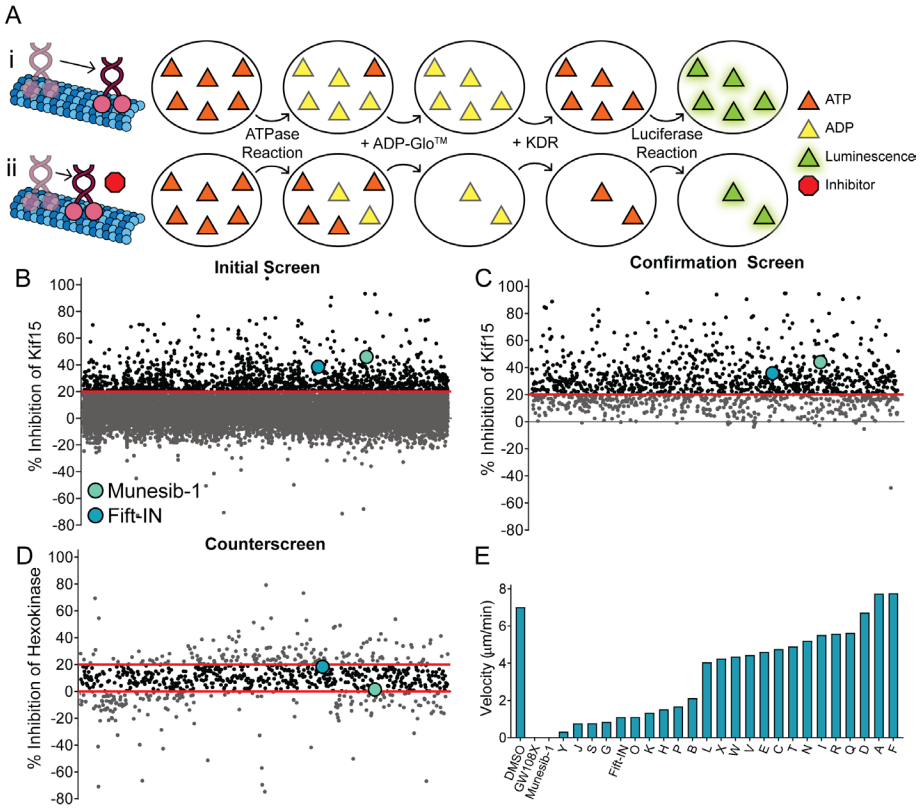

FIGURE 1: Overview of KIF15 inhibitor screen. (A) Schematic of ADP-Glo Kinase Assay used for screening. (i) KIF15-N420 is incubated with taxol-stabilized microtubules and 20 µM ATP (orange); ATP is hydrolyzed to ADP (yellow) via KIF15's ATPase activity; unhydrolyzed ATP is depleted by the ADP-Glo reagent; ADP is converted back into ATP by the KDR, which is coupled to a luciferase reaction to produce quantifiable luminescence (green). (ii) In the presence of a KIF15 inhibitor, KIF15's ATPase activity is reduced, resulting in less luminescence produced downstream. (B) Results of the initial round of screening of 23,552 compounds from the MB 24K library, quantifying the % inhibition of KIF15 compared with the control. Each dot represents one compound. The red bar represents the 20% inhibition threshold above which hits were deemed active against KIF15. The results of Munesib-1 and Fift-IN are indicated in green and blue, respectively. (C) Results of the confirmation screen of 1330 compounds. Each dot represents the average % inhibition of three replicates for each compound. As in B, the red bar indicates the threshold above which hits were deemed active. (D) Results of the counterscreen of 864 compounds tested against Hexokinase. Compounds that resulted between 0 and 20% inhibition of Hexokinase were deemed inactive, indicated by the red bars. (E) Average microtubule gliding velocity of KIF15-N700 for each of the 25 compounds tested. DMSO was used as a negative control; 30 µM GW108X was used as a positive control. Each compound was tested in singlicate with $n = 10$ for each compound.

this round to include any compounds showing between 0 and 20% inhibition of hexokinase activity. Of 864 compounds tested, 502 exhibited no inhibitory activity against hexokinase.

From this list of 502 compounds that showed specific activity against KIF15, we further eliminated any compounds known for binding proteins promiscuously or that contained residues known to be reactive or toxic in vivo. We then ranked the remaining compounds that passed the counterscreen by their activity against KIF15 and selected the 120 most potent compounds for concentration-response testing; 95 of the 120 compounds tested showed a concentration response relationship; 25 of the best performing compounds were then selected for further testing using microtubule gliding assays.

For gliding assays, we used a longer dimeric KIF15 construct, KIF15-N700, which powers robust microtubule movement (Sturgill *et al.*, 2014). Of the 25 compounds tested, we identified several that robustly inhibit the microtubule gliding ability of KIF15 at 30 µM (Figure 1E). We selected two compounds for further testing and designated them as Munesib-1 (named for mu, the 15th letter of the Greek alphabet) and Fift-IN (as in KIF-*fift*een *in*hibitor) (Figure 2A). These two compounds were chosen due to their strong activity and their favorable concentration response curves (CRCs).

Munesib-1 and Fift-IN are potent and specific KIF15 inhibitors

We implemented two methods for concentration-response analysis, microtubule gliding assays (Figure 2B) and an enzyme-coupled ATPase assay. The IC50 values of Munesib-1 and Fift-IN were 2.8 and 20.9 µM, respectively, in the ATPase assay (Figure 2, C and D), while microtubule gliding assays yielded IC_{50} values for Munesib-1 and Fift-IN of 0.4 and 5 µM, respectively (Figure 2, E and F). The ATPase assay tests the properties of single motors, whereas the microtubule gliding assay examines the activity of ensembles of motors. It is, therefore, not unexpected to obtain different estimated IC_{50} values from these two methods. Nonetheless, both methods reflect an order of magnitude of difference in IC_{50}s between the two compounds.

Both compounds have a relatively low "leadlike" molecular weight (351 and 312, respectively). This makes them both amenable to medicinal chemistry optimization, thus allowing significant headroom for incorporation or modification of functional groups. From a purely structural point of view, Munesib-1 is the preferable scaffold for optimization due to its already low ClogP (2.14 vs. 5.68, calculated using ChemDraw) and readily modifiable carboxylic ester and 2-thiomethyl substituted pyrimidine. Fift-IN is significantly more lipophilic and thus is more limited in selection of modifications due to the need to, at the very least, maintain lipophilicity at its current level.

To assess the reversibility of Munesib-1 and Fift-IN, we performed washout experiments using the microtubule gliding assay. We imaged microtubule gliding of KIF15-N700 for 1 min, then added either DMSO or a KIF15 inhibitor to the flow cell and imaged gliding for another minute, and then washed out the inhibitor and imaged for one final minute (Figure 2G). Microtubule gliding velocity was unaffected by the addition or removal of DMSO. Gliding was fully abrogated by the addition of 24 µM Munesib-1 to the flow cell, but gliding velocity was nearly restored to baseline after its removal, indicating that Munesib-1 is a reversible inhibitor (Figure 2H). However, gliding was still inhibited by >90% after washout of 100 µM Fift-IN, which suggests that Fift-IN is not reversible (Figure 2H). From this assay, it is not possible to determine whether Fift-IN actually binds to KIF15 in a chemically irreversible way, or if it dissociates

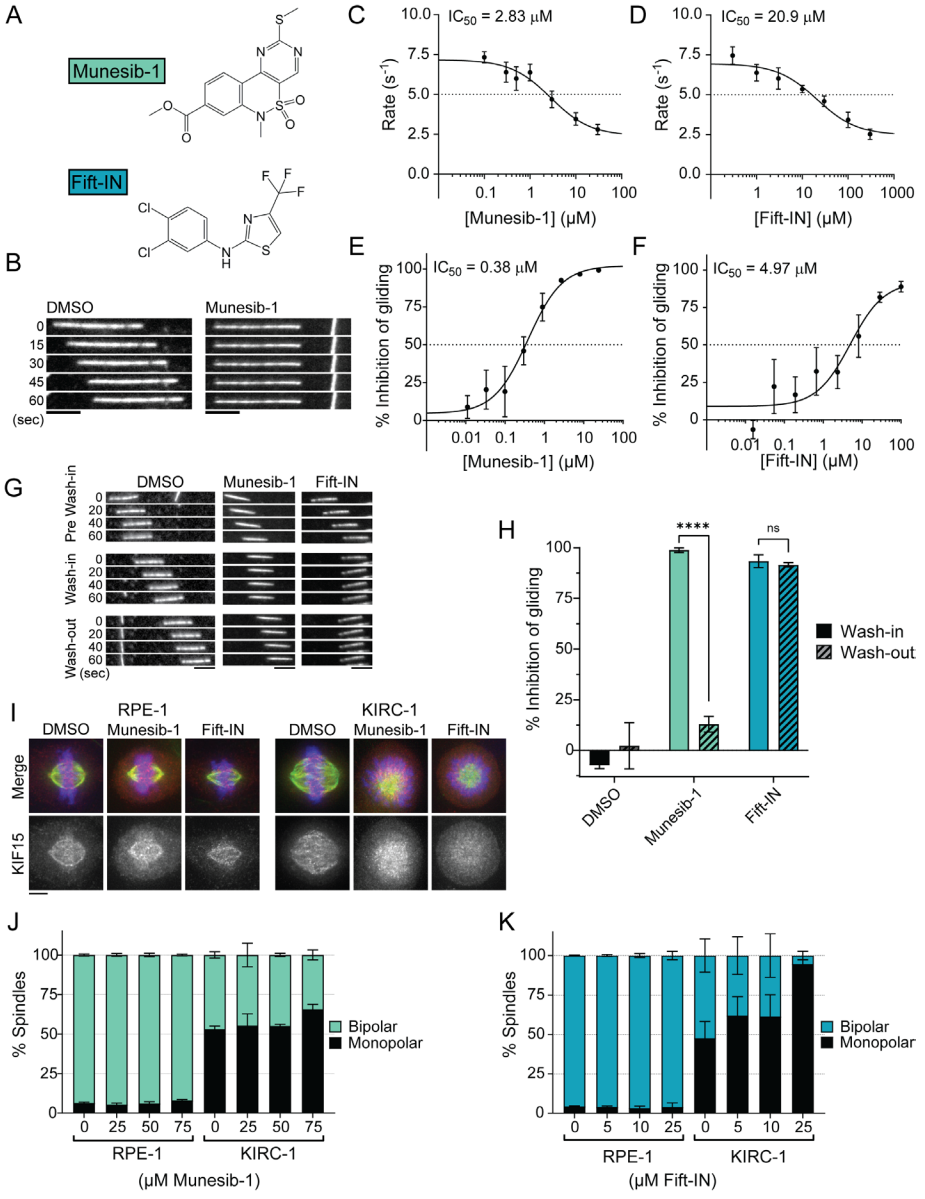

FIGURE 2: Munesib-1 and Fift-IN potently inhibit Kif15 both in vitro and in cells. (A) Chemical structures of Munesib-1 (top) and Fift-IN (bottom). (B) Representative montage of a fluorescently labeled stabilized microtubule in gliding assay utilizing KIF15-N700 treated with either DMSO (left) or 24 μM Munesib-1 (right). Time of each frame is indicated on the left in seconds. Scale bar, 5 μm. (C) CRC generated from ATPase assays with Munesib-1 over a range of eight concentrations from 0.1 to 30 μM. Each concentration was repeated for a total $n = 3–9$. Error bars show ± SEM. (D) CRC generated from ATPase assays with Fift-IN over a range of eight concentrations from 0.3 to 300 μM. Each concentration was repeated for a total $n = 6–9$. Error bars show ± SEM. (E) CRC generated from microtubule gliding assays with Munesib-1 over a range of eight concentrations from 10 nM to 30 μM. Each concentration was repeated in triplicate, $n \geq 50$ for each replicate. Error bars show ± SEM. (F) CRC generated from gliding assays with Fift-IN over a range of eight concentrations from 10 nM to 100 μM. Each concentration was repeated in triplicate, $n \geq 50$ for each replicate. Error bars show ± SEM. (G) Representative montage of a microtubule from a washout assay with the addition of either DMSO (left), 24 μM Munesib-1 (middle), or 100 μM Fift-IN (right). Microtubule motility is shown before drug was added ("Pre Wash-in," top), after drug was added ("Wash-in," middle), and after drug was washed out ("Wash-out," bottom). Time elapsed from the first frame of each phase is indicated on the left in seconds. Scale bar, 5 μm. (H) Quantification of washout experiment showing % inhibition of gliding velocity of KIF15 after addition of drug ("Wash-in," solid bars) and after washout of drug ("Wash-out," hatched bars) for the addition and washout of DMSO, 24 μM Munesib-1, or 100 μM Fift-IN. Each compound was tested in triplicate, $n \geq 20$ for each replicate. Error bars show ± SEM. Statistical results are shown for an unpaired *t* test; ns, no significance; $^{****}P < 0.0001$. (I) Max intensity z-projections of RPE-1 cells (left) and KIRC-1 cells (right) treated with either DMSO, 50 μM Munesib-1, or 25 μM Fift-IN. Cells were stained with antibodies targeting KIF15 (red) and tubulin (green) and were counterstained with Hoechst 33342 (blue). Scale bar, 5 μm. (J) Quantification of preanaphase spindles in either monopolar or bipolar states in RPE-1 (left) or KIRC-1 (right) cells treated with increasing concentrations of Munesib-1. Concentration is indicated on the bottom of each bar in μM. Each concentration was tested in triplicate, $n = 100$ for each replicate. Error bars show ± SEM. (K) Quantification of preanaphase spindles in either monopolar or bipolar states in RPE-1 (left) or KIRC-1 (right) cells treated with increasing concentrations of Fift-IN. Concentration is indicated on the bottom of each bar in μM. Each concentration was tested in triplicate, $n = 100$ for each replicate. Error bars show ± SEM.

very slowly from its target site on the motor.

We next analyzed the effects of Munesib-1 and Fift-IN on spindle assembly in cells by quantifying the number of monopolar spindles in *TP53*$^{-/-}$ RPE-1 and KIRC-1 cells (Sturgill and Ohi, 2013) that have been treated with the compounds. KIF15 is nonessential in cells when Eg5 is present, and KIF15 inhibitors should, therefore, have little to no effect on RPE-1 cells. However, RPE-1-derived KIRC-1 cells are cultured in saturating amounts of the K5I STLC (Debonis *et al.*, 2004) and depend on KIF15 for their Eg5-independent spindle assembly pathway (Sturgill and Ohi, 2013). Thus inhibition of KIF15 should block spindle assembly in KIRC-1 cells, resulting in an increase in monopolar preanaphase structures (Figure 2I). Since KIRC-1 spindles proceed through a monopolar intermediate before bipolarizing in early metaphase, KIRC-1 cells exhibit a high baseline rate of monopolarity in untreated cells; however, depletion or inhibition of KIF15 is sufficient to raise this monopolarity index by a quantifiable amount (Sturgill and Ohi, 2013). Both compounds had little effect on spindle morphology in RPE-1 cells (Figure 2, J and K) but caused KIRC-1 cells to have a concentration-dependent increase in the monopolarity index relative to cells treated with DMSO. Notably, treatment with Fift-IN produced nearly 100% monopolar spindles at 25 μM (Figure 2K), whereas the effects of Munesib-1 were comparatively modest, even when the compound was present at 75 μM (Figure 2G). This behavior is opposite of the trend we observed in vitro, and we hypothesized that Munesib-1 may be less effective in cells due to reduced solubility. Indeed, we noted that

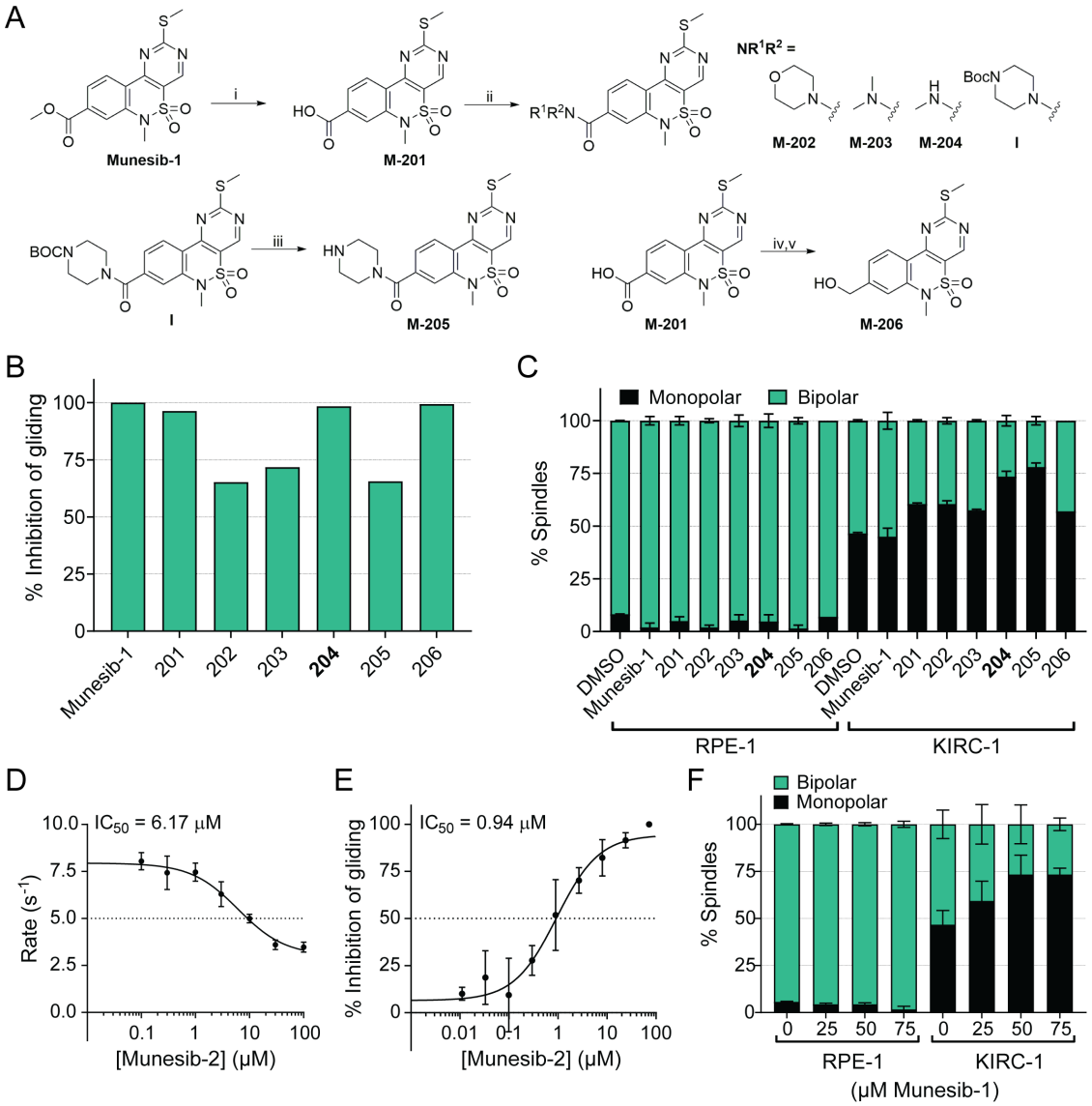

FIGURE 3: Chemical derivatives of Munesib-1 increase potency against KIF15 in cells. (A) Overview of chemical derivatives of Munesib-1 that were synthesized and tested. Reagents and conditions are as follows: 1) LiOH, DMF/H2O, 25°C; 2) HATU, DIPEA, R1R2NH, DMF, 60°C; 3) TFA, CH2Cl2, RT; 4) oxalyl chloride, CH2Cl2, RT; 5) LAH, THF, 0°C, RT. (B) Quantification of the % inhibition of KIF15 microtubule gliding activity induced by each chemical derivative tested at 25 μm. Each compound was tested in singlicate, $n \geq 50$ for each compound. (C) Quantification of preanaphase spindles in either monopolar or bipolar states in RPE-1 (left) or KIRC-1 (right) cells treated with each chemical derivative as well as the parent compound. Each compound was tested at 25 μM in duplicate, $n = 100$ for each replicate. Error bars show ± SEM. (D) CRC generated from ATPase assays with Munesib-2 (M-204) over a range of eight concentrations from 0.1 to 100. Each concentration was repeated for a total $n = 4–7$. Error bars show ± SEM. (E) CRC generated from microtubule gliding assays with Munesib-2 over a range of nine concentrations from 10 nM to 30 μM. Each concentration was tested in triplicate, $n \geq 50$ for each replicate. Error bars show ± SEM. (F) Quantification of preanaphase spindles in either monopolar or bipolar states in RPE-1 (left) or KIRC-1 (right) cells treated with increasing concentrations of Munesib-2. Concentration is indicated on the bottom of each bar in μM. Each concentration was tested in triplicate, $n = 100$ for each replicate. Error bars show ± SEM.

Munesib-1 often precipitated in culture media while assessing its effects on cells. Interestingly, Munesib-1 and Fift-IN were less effective at inducing monopolar spindle assembly in HeLa-derived KIRC-2 cells (Sturgill *et al.*, 2016). While they had little effect on the parental HeLa line, both inhibitors failed to substantially increase the monopolarity index in KIRC-2 cells (Supplemental Figure S3, A and C) when tested at the same concentrations that were used in RPE-1-derived KIRC-1 cells (Figure 2, J and K).

Munesib-2 is more potent in cells due to increased solubility

To increase the solubility of Munesib-1, we made changes to its structure that are predicted to increase solubility, resulting in six chemical derivatives that we designated M-201–M-206 (Figure 3A). Munesib-1 (MolPort) was hydrolyzed with lithium hydroxide in aqueous DMF to give M-201 in 71% yield. Amide coupling of compound I using HATU/N,N-diisopropylethylamine in DMF gave M-202, M-203, M-204, and I in moderate to good yields. The Boc group of

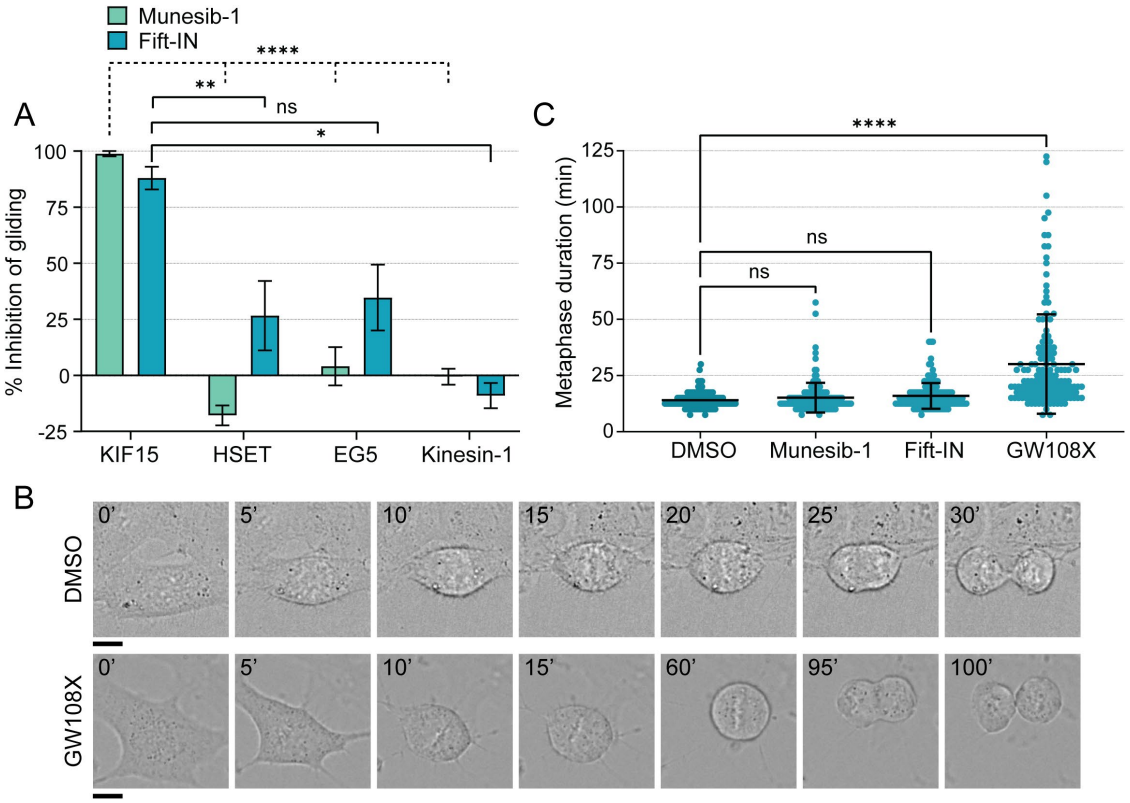

FIGURE 4: Munesib-1 and Fift-IN are selective KIF15 inhibitors. (A) Quantification of % inhibition of microtubule gliding compared with DMSO control, for each of the motors indicated when treated with either 24 μM Munesib-1 or 100 μM Fift-IN. Each motor and compound were tested in triplicate, $n \geq 50$ for each replicate. Error bars show ± SEM. Statistical results are shown for a one-way ANOVA with Tukey's multiple comparisons test; ns, no significance; $*P < 0.05$; $**P < 0.01$; $****P < 0.0001$. (B) Schematic of mitotic progression of RPE-1 cells treated either with DMSO (top) or 25 μM GW108X (bottom). Images were collected via time-lapse microscopy. Time in minutes is indicated relative to the first frame. Scale bar, 5 μm. (C) Quantification of metaphase duration for RPE-1 cells treated with the indicated inhibitor (Munesib-1 used at 50 μM, Fift-IN and GW108X used at 25 μM). Time was quantified in minutes from metaphase plate formation until anaphase onset. Each dot represents one measurement. Each concentration was tested in triplicate, $N = 50$ cells for each replicate. Error bars show ± SEM. Statistical results are shown for a one-way ANOVA with Tukey's multiple comparisons test; ns, no significance; $****P < 0.0001$.

compound I was removed by treatment with TFA in methylene chloride to give M-205. Finally, M-201 was reduced via sequential treatment with oxalyl chloride in methylene chloride followed by reduction with lithium aluminum hydride in THF to give compound M-206.

We first assessed the potency of these chemical derivatives using the microtubule gliding assay, selecting 25 μM as a starting point since the parent compound completely eliminates KIF15-driven microtubule gliding at this concentration. While all compounds displayed greater than 50% inhibition of KIF15 when tested at 25 μM, three derivatives (M-201, M-204, and M-206) blocked KIF15 activity as effectively as Munesib-1 (Figure 3B). We then tested all six derivatives in cells, again using all compounds at 25 μM. While none of the compounds produced a change in spindle morphology in RPE-1 cells, we observed that two derivatives (M-204 and M-205) substantially increased the monopolarity index in KIRC-1 cells compared with the parent compound (Figure 3C). We thus selected compound M-204, designated as Munesib-2, for further evaluation since it matched Munesib-1 in the gliding assay and improved upon Munesib-1's effects in cells. Munesib-2 is slightly less potent than the parent compound Munesib-1 in vitro, with an IC_{50} ~2-fold higher (0.8 μM and 0.4 μM, respectively, via microtubule gliding assays; 6.2 and 2.8 μM, respectively, via steady-state ATPase assays). However, Munesib-2 substantially increased efficacy in cells; 75 μM Munesib-2 resulted in more than 80% monopolar spindles in KIRC-1 cells, while an equal concentration of Munesib-1 yielded less than 70% monopolar spindles. Evidently, Munesib-2 has increased potency in cells without losing much efficacy in vitro. Finally, Munesib-2 showed the same low efficacy as Munesib-1 and Fift-IN in HeLa-derived KIRC-2 cells (Supplemental Figure S3B).

Munesib-1 and Fift-IN show reduced off-target effects compared with GW108X

After evaluating the potency of Munesib-1 and Fift-IN against KIF15, we assessed their specificity. We first tested the compounds against three other motors in the microtubule gliding assay using concentrations of Munesib-1 and Fift-IN that completely abrogate KIF15-driven microtubule gliding. We selected HSET and Eg5, two other mitotic kinesins that are structurally distinct from KIF15 despite performing similar functions, and K560, a truncated form of kinesin-1. While both compounds robustly inhibited KIF15 at the selected concentrations, neither substantially inhibited the microtubule gliding ability of the three other motors, indicating that these compounds are specific for KIF15 (Figure 4A).

We next evaluated the effects of Munesib-1 and Fift-IN on mitotic progression in RPE-1 cells by filming the progression of drug-treated cells through mitosis with differential interference contrast

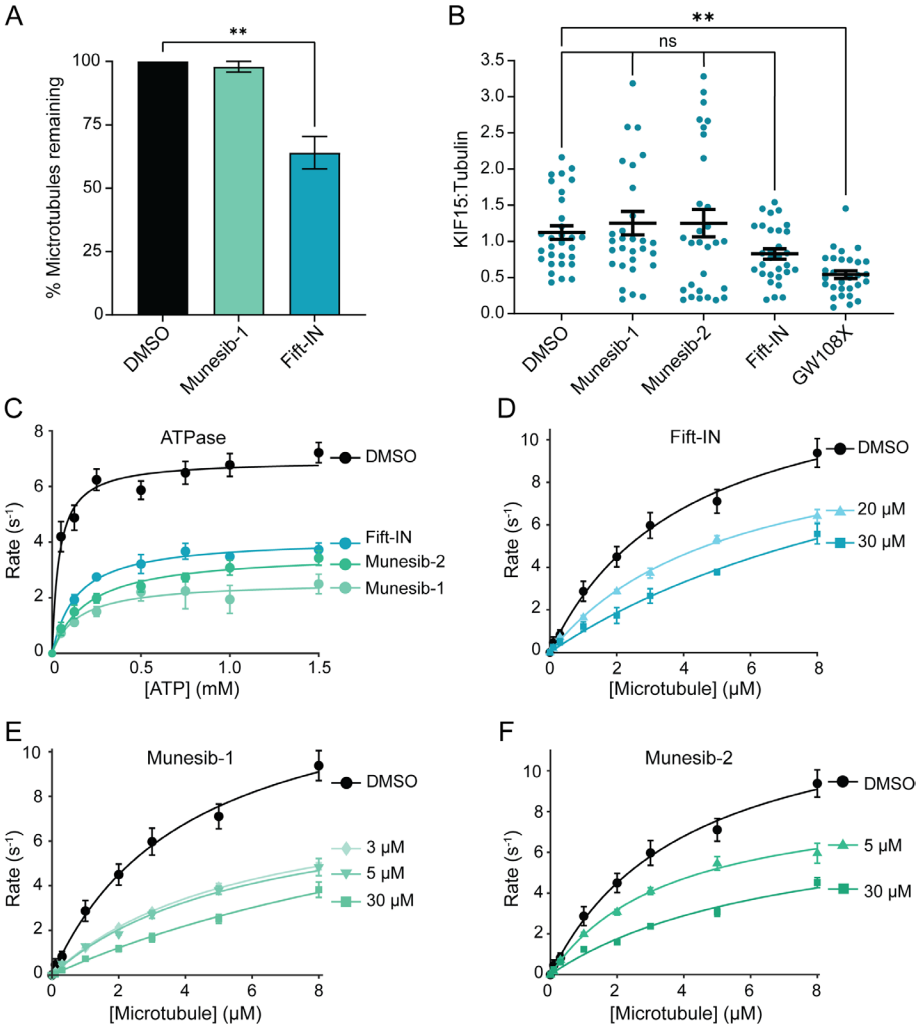

FIGURE 5: Munesib and Fift-IN have distinct mechanisms of inhibition of KIF15. (A) Quantification of the percentage of microtubules that remain bound to the coverslip after 1 min postdrug addition for DMSO, 24 µM Munesib, or 100 µM Fift-IN. Experiment was repeated in triplicate; $n \geq 50$ for each replicate. Statistical results are shown for a one-way ANOVA with Tukey's multiple comparisons test; $^{**}P < 0.01$. (B) Quantification of KIF15 on metaphase spindles in RPE-1 cells treated with either DMSO or the indicated compound (GW108X and Fift-IN used at 25 µM, Munesib-1 and -2 used at 50 µM). Each dot represents one measurement. Experiment was repeated in triplicate, $n = 10$ for each replicate. Statistical results are shown for a one-way ANOVA with Tukey's multiple comparisons test; ns, no significance; $^{**}P < 0.01$. Error bars show ± SEM. (C) Michaelis-Menten plots generated from ATP-dependent ATPase assays with DMSO, Fift-IN, Munesib-1, and Munesib-2 over a range of eight concentrations from 0 to 1.5 mM of ATP. Michaelis-Menten fits using kobs = (kcat*[ATP])/(Km+[ATP]) are weighted by 1/SEM. Each concentration was repeated for a total $n = 5–7$ and plotted as mean ± SEM. (See Table 1 for kcat and Km values.) (D) Michaelis-Menten plots generated from Microtubule-dependent ATPase assays, over a range of eight concentrations from 0 to 8 µM of tubulin, in the presence of DMSO, 20 µM or 30 µM Fift-IN. Michaelis-Menten fits using kobs = (kcat*[Mt])/(Km+[Mt]) are weighted by 1/SEM. Each microtubule concentration was repeated for a total $n = 6–9$ and plotted as mean ± SEM. (E) Michaelis-Menten plots generated from Microtubule-dependent ATPase assays, over a range of eight concentrations from 0 to 8 µM of microtubules, in the presence of DMSO, 3, 5, or 30 µM Munesib-1. Michaelis-Menten fits using kobs = (kcat*[Mt])/(Km+[Mt]) are weighted by 1/SEM. Each microtubule concentration was repeated for a total $n = 6–9$ and plotted as mean ± SEM. F) Michaelis-Menten plots generated from Microtubule-dependent ATPase assays, over a range of eight concentrations from 0 to 8 µM of microtubules, in the presence of DMSO, 5 µM or 30 µM Munesib-2. Michaelis-Menten fits using kobs = (kcat*[Mt])/(Km+[Mt]) are weighted by 1/SEM. Each microtubule concentration was repeated for a total $n = 6–9$ and plotted as mean ± SEM. (D–F) The DMSO control curve is the same data set replotted for direct comparison. (See Table 2 for kcat and Km values.)

microscopy (Figure 4B). We performed this analysis because we observed that the KIF15 inhibitor GW108X, a known kinase inhibitor (Elkins *et al.*, 2016), increased the time needed for cells to enter anaphase following chromosome alignment at the metaphase plate (Figure 4C). GW108X-treated RPE-1 cells also exhibited a peculiar spindle oscillation phenotype, in which the spindle rocked back and forth prior to anaphase onset (Figure 4B). We speculate that these effects are a result of promiscuous kinase inhibition. We imaged RPE-1 cells treated with saturating doses of Munesib-1 or Fift-IN and quantified the time between metaphase plate formation and anaphase onset (Figure 4C). Compared with the significant increase in metaphase duration with GW108X treatment, we observed no significant change in metaphase timing with treatment of either Munesib-1 or Fift-IN. Combined with the gliding assay utilizing other motors, these results suggest that Munesib-1 and Fift-IN are selective KIF15 inhibitors and improve upon the limited specificity of GW108X.

Fift-IN decreases microtubule-binding activity of KIF15

To determine whether Munesib-1 and Fift-IN affect the ability of KIF15 to bind to microtubules, we analyzed the effect on microtubule binding immediately after the addition of each compound during microtubule gliding assays (Figure 5A). Compared with the DMSO control, the addition of Fift-IN induced a significant reduction in the number of microtubules bound to the coverslip via KIF15, whereas Munesib-1 had little effect on binding. We looked at this further in cells by measuring the relative amounts of KIF15 on spindle microtubules in RPE-1 cells in metaphase (Figure 5B). Similar to our in vitro results, treatment of cells with a saturating dose of Fift-IN significantly reduced the amount of KIF15 on the spindle, while Munesib-1 again had little effect. This effect on spindle binding with Fift-IN was similar to the effect seen with the addition of GW108X, which is consistent with its known allosteric inhibition of microtubule binding (Dumas *et al.*, 2019). These results suggest that Fift-IN also competes with microtubule binding, whereas it is unclear how Munesib-1 inhibits KIF15 activity. The putative difference in mechanism of inhibition implies that Munesib-1 and Fift-IN may have distinct binding sites on the motor domain of KIF15.

To further characterize the mechanism of action of these inhibitors, we used an enzyme-coupled assay to analyze the impact of

Compound	k_{cat} (s^{-1})	K_m (μM)
DMSO	6.9 ± 0.6	40 ± 25
Fift-IN	4.1 ± 0.4	139 ± 41
Munesib-1	2.6 ± 0.4	146 ± 60
Munesib-2	3.6 ± 0.4	200 ± 82

TABLE 1: ATP-dependent ATPase Michaelis-Menten fits. Corresponding values for the Michaelis-Menten fits in the plots in Figure 5C. Reported values for k_{cat} and K_M are fit ± 95% confidence interval. All compounds are 30 μM and the DMSO control was done using equal volume.

the inhibitors on the steady-state ATPase kinetics of KIF15. As KIF15 requires both ATP and microtubules to stimulate its ATPase activity, there are two potential substrate sites for competitive binding, the nucleotide-binding pocket and the microtubule-binding interface. Thus we varied both the ATP and the microtubule concentrations to determine whether the drugs compete with the binding of one or both of the substrates to KIF15. In the ATP-dependent assay at 3 μM microtubules, we observed a decrease in the k_{cat} with a similar K_m for all three compounds, relative to the DMSO control, indicating that the inhibitors are all noncompetitive with ATP (Figure 5C; Table 1).

In the microtubule-dependent ATPase assay at 2 mM ATP, we find that Fift-IN binds competitively with microtubules. In the Michaelis-Menten plot, the k_{cat} is maintained across all concentrations of Fift-IN, whereas the K_m increases with increasing Fift-IN concentration (Figure 5D; Table 2). This conclusion is confirmed by two additional analysis methods. First, when plotted as a Lineweaver-Burk with fits weighted by inverse of the relative error of the mean, the curves of all Fift-IN concentrations intersect at the y intercept, consistent with competitive inhibition (Supplemental Figure S4A). Second, we implemented global fits of the data across all inhibitor concentrations to three inhibition models: mixed, competitive, and noncompetitive (Supplemental Figure S4, D, G, and J). Because the mixed model has more degrees of freedom, we can consider this fit as an example of "best fit" and compare the sum of squares for the competitive and noncompetitive fits to that of the mixed model. In the case of Fift-IN, the competitive fit more closely resembles the mixed model fit, indicating that Fift-IN binds the microtubule-binding interface competitively with microtubules.

The Michaelis-Menten plot for the microtubule dependence of KIF15 ATPase in the presence of Munesib-1 is less conclusive, with no obvious trend suggesting a shift in K_m or k_{cat} (Figure 5E; Table 2). In addition, the Lineweaver-Burk plot exhibits a disagreement between the higher concentration (30 μM) and the lower concentrations (3 and 5 μM) of Munesib-1 (Supplemental Figure S4B). The lower concentrations suggest noncompetitive inhibition with microtubules, whereas the highest concentration suggests competitive inhibition. Furthermore, by implementing the global fits of the Munesib-1 data to the three models, we find that the data do not conform to a particular model and that all model fits generate a large sum of squares errors (Supplemental Figure S4, E, H, and K). We hypothesized that the solubility issues of Munesib-1 contributed to this indeterminate result of microtubule competition; thus we implemented this same assay to evaluate its more soluble derivative, Munesib-2. This derivative exhibits a decrease in k_{cat} with increasing compound concentration and values of K_m for microtubules similar to the DMSO control (Table 2). All three analysis methods of the Munesib-2 data agree; therefore, we conclude that Munesib-2 is noncompetitive with microtubules (Figure 5F; Supplemental Figure S4, C, F, I, and L).

Compound	Compound concentration	k_{cat} (s^{-1})	K_m (μM)
DMSO	Equal volume*	13.8 ± 2	4.1 ± 1
Fift-IN	20 μM	10.8 ± 2	5.4 ± 1
	30 μM	14.2 ± 9	13.2 ± 11
Munesib-1	3 μM	8.5 ± 1	5.9 ± 1
	5 μM	8.2 ± 3	6.1 ± 3
	30 μM	11.6 ± 6	17 ± 10
Munesib-2	5 μM	9.0 ± 1	4 ± 1
	30 μM	8.1 ± 5	7 ± 7

TABLE 2: Microtubule-dependent ATPase Michaelis-Menten fits. Corresponding values for the Michaelis-Menten fits in the plots in Figure 5 D-F. Reported values for k_{cat} and K_M are fit ± 95% confidence interval. DMSO control was done using the same volume as used in the 30 μM trial.

Fift-IN synergizes with the K5I STLC to prevent the acquisition of drug resistance

Last, we analyzed the effect of KIF15 inhibition by Fift-IN on the ability of cells to acquire resistance to STLC, a commonly used K5I. *TP53*$^{-/-}$ RPE-1 cells were cultured for 24 d in either normal DMEM medium or medium containing 10 μM STLC, 50 μM Munesib-2, 10 μM Fift-IN, or a combination of STLC and either Munesib-2 or Fift-IN together. As expected, neither KIF15 inhibitor alone had little effect on cell growth compared with the control (Figure 6, A–C). STLC killed the majority of *TP53*$^{-/-}$ RPE-1 cells, but some cells acquired resistance to STLC and grew to form colonies (Figure 6D, see zoomed-in insets). However, combined treatment of STLC and either Munesib-2 or Fift-IN substantially decreased the number of resistant colonies that arose (Figure 6, E and F, see zoomed-in insets), showing that inhibition of KIF15 activity sensitizes cells to K5I treatment. This result is consistent with the notion that Fift-IN is a small molecule that acts specifically to block KIF15 activity during mitosis.

DISCUSSION

Chemical inhibitors of kinesins represent valuable tools for the cell biology community and can be used to improve our understanding of the mechanisms that govern spindle assembly and function. Most recently, the kinesin-8 Kif18A has been postulated to be an Achilles' heel of cancer cells that are chromosomally unstable (Cohen-sharir *et al.*, 2021; Marquis *et al.*, 2021; Quinton *et al.*, 2021) and the field awaits Kif18A inhibitors to evaluate the validity of this chemotherapeutic approach in patients. Using high-throughput screening, we identified two novel KIF15 inhibitor scaffolds that potently inhibit KIF15 activity both in vitro and in vivo. These compounds add to our growing toolbox of KIF15 inhibitors, which include the oxindole GW108X (Dumas *et al.*, 2019) and KIF15-IN-1 (Milic *et al.*, 2018). Our motivation to isolate KIF15 inhibitors is that human cells can escape the cytotoxic effects of K5Is by switching to an alternative spindle assembly pathway that depends on KIF15. We show here that, similar to genetic deletion of KIF15, Fift-IN reduces the ability of human cells to acquire resistance to the K5I STLC. This result validates the hypothesis that combined treatment of cells with a K5I and KIF15 inhibitor will combat the ability of cells to acquire K5I resistance.

Although Munesib-1 and Fift-IN both block KIF15 activity, the two molecules are structurally distinct. While both molecules selectively target KIF15, Munesib-1 exhibits roughly 10-fold stronger inhibitory action against KIF15 in both in vitro ATPase and microtubule gliding assays. Intriguingly, the opposite trend is observed in

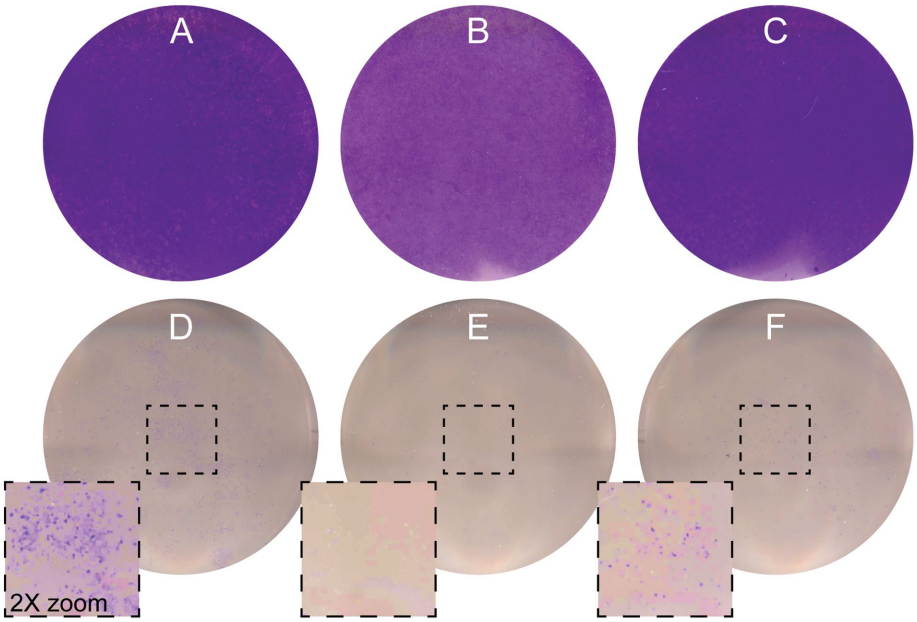

FIGURE 6: STLC and KIF15 inhibitors synergize to prevent adaptation to K5Is. RPE-1 cells grown to 80% confluency and treated for 24 d with (A) no compound, (B) 50 µM Munesib-1, (C) 12 µM Fift-IN, (D) 10 µM STLC, (E) 10 µM STLC and 50 µM Munesib-2, or (F) 10 µM STLC and 10 µM Fift-IN. Colonies were then stained with crystal violet. Insets in D–F are enlarged and enhanced to show the difference in growth between cells treated with just STLC compared with the addition of Munesib-2 or Fift-IN. Experiment was done in singlicate ($n = 1$).

cell-based assays, with Fift-IN maximally abrogating bipolar spindle formation at much lower concentrations than Munesib-1. This discrepancy may be due to Munesib-1's poor solubility, and indeed, substantial in vivo potency was gained by chemical modifications that increased solubility, as indicated by the results of Munesib-2. This increase in potency still did not outmatch the high activity of Fift-IN in cells, and it remains unclear why Munesib-2 is not as efficacious in cells. Future pharmacokinetics studies or permeability assays may elucidate whether the discrepancy in efficacy stems from differences in drug uptake or efflux between the two compounds. It is also possible that Fift-IN dissociates from KIF15 very slowly, as suggested by its irreversible inhibition of KIF15-driven microtubule gliding.

An important quality of Munesib-1 and Fift-IN is their selectivity. Both compounds have little to no effect on three other kinesins, despite high sequence homology of kinesin motor domains. Additionally, both inhibitors appear to be more on target compared with our previously published KIF15 inhibitor, GW108X, which inhibits several kinases in addition to KIF15 (Elkins *et al.*, 2016). The most noticeable phenotype suggestive of GW108X's off-target activity is a significant increase in the time from metaphase plate formation to anaphase onset in RPE-1 cells; as mitotic arrest can increase the chances of cells undergoing apoptosis (Gascoigne and Taylor, 2009), this effect is undesirable for cells that should otherwise be unaffected by KIF15 inhibition. The metaphase duration of cells treated with either Munesib-1 or Fift-IN was similar to that of DMSO-treated cells, and thus we conclude that these compounds act primarily on KIF15.

Our enzymology data shed light on the mechanism of action of Munesib-1 and -2 and Fift-IN. Kinesin inhibitors typically work via one of two mechanisms, either 1) impairing ATPase activity by inhibiting nucleotide binding, hydrolysis, or release or 2) impairing microtubule binding. From analyzing in vitro microtubule binding, spindle localization in cells, and steady-state kinetics, Fift-IN appears to inhibit microtubule binding of KIF15. In contrast, Munesib-1 and -2 do not appear to have a strong effect on microtubule binding in these assays. This difference in mechanism may contribute to the discrepancy in in vitro and cell-based activity between the two compounds.

Interestingly, while Munesib-1, -2, and Fift-IN block spindle assembly in RPE-1-derived KIRC-1 cells, they are substantially less effective against HeLa-derived KIRC-2 cells. In Eg5-independent spindle assembly, KIF15 localizes to kinetochore–microtubules to facilitate separation of the spindle poles (Sturgill and Ohi, 2013; Sturgill *et al.*, 2016). The half-lives of this subpopulation of microtubules differ significantly between cell lines and are notably much higher in HeLa cells than in RPE-1 cells (Bakhoum *et al.*, 2009; Gayek *et al.*, 2014). We speculate that Munesib-1, -2, and Fift-IN have reduced activity in HeLa versus RPE-1 KIRCs because the longer-lived kinetochore–microtubules of HeLa cells promote KIF15-driven spindle assembly. More work is necessary to test this hypothesis, but this is clearly an important area for future study because cancer cells are known to have long-lived kinetochore–microtubules (Bakhoum *et al.*, 2009).

In summary, Munesib-1 and Fift-IN are powerful tools for the cell biology community to study the complex forces involved in mitotic spindle assembly. Indeed, KIF15 inhibitors have already proven effective for studying microtubule organization in the spindle (Begley *et al.*, 2021), and there are numerous potential applications for their use in studying KIF15's force contribution to spindle assembly and maintenance that thus far have relied upon genetic manipulation such as RNA interference. The difference in activity of Munesib-1 and Fift-IN can also be harnessed for more specific applications; Munesib-1 is a potent inhibitor of KIF15 in vitro, whereas Fift-IN robustly inhibits KIF15 activity in cells. The improvement of cell-based activity of Munesib-2 without significant loss of in vitro potency also makes it a good tool for use in both settings. Finally, these compounds will enable testing of Eg5 and KIF15 as a combined anticancer drug target. Combining Fift-IN or Munesib-2 with STLC, a K5I, decreases the ability of cells to acquire resistance to STLC, highlighting the centrality of KIF15 to K5I resistance mechanisms. Future experiments with more in vitro cancer cell lines and in vivo tumor models can further illuminate the efficacy of combining K5Is and KIF15 inhibitors as an anticancer therapy.

MATERIALS AND METHODS

Request a protocol through *Bio-protocol*.

ADP-Glo kinase reaction

The ADP Glo Kinase Assay kit (Promega) was used to quantify the ATPase activity of KIF15-N420 and was adapted for use in high-throughput screening, as previously described (Dumas *et al.*, 2019); 23,552 compounds were queried from the Maybridge 24k library of small molecules. Compounds were screened in 24 × 16 (384) well plates; for each plate, one compound was added to each well in columns 3–22, just DMSO was added to wells in columns 1–2 to serve as a negative control (representing the baseline ATPase rate of KIF15), and ATP was excluded from wells in columns 23–24 to

serve as a positive control (mimicking 100% inhibition of ATPase activity).

Ten microliters of Motor and MT solution (100 nM His_6-KIF15-N420 (Sturgill *et al.*, 2014) and 1 μM Taxol-stabilized microtubules in screening buffer (10 mM K-HEPES [pH 7.7], 100 mM KCl, 1 mM DTT, 10 mM $MgCl_2$, and 5 μM Taxol) was dispensed into each well of a 384 well plate using a Multidrop Combi liquid dispenser (Thermo Fisher Scientific); 200 nl of each compound (2 mM stock in DMSO, final concentration of 20 μM) was added to wells in columns 3–22 of each plate using a Biomek FX pintool (Beckman Coulter); no compound was added to wells in columns 1–2 and 23–24. Plates were incubated for 15 min at room temperature (RT); 10 μl ATP solution (20 μM MgATP in screening buffer) was dispensed to wells in columns 1–22; 10 μl screening buffer was dispensed to wells in columns 23–24. Plates were incubated 20 min at RT; 5 μl of ADP-Glo reagent was added to every well, and the plate was incubated 40 min at RT. Finally, 10 μl kinase detection reagent (KDR) was added to every well, and the plate was incubated 30 min. Luminescence was quantified using an Envision 2104 Multilabel plate reader (PerkinElmer). The percentage of inhibition of ATPase activity was calculated for each compound by normalizing to the average luminescence of the positive control wells for each plate.

To estimate the robustness of this assay, the Z′ score was calculated using the equation:

$$Z' = 1 - \frac{3 * \sigma_{C+} + 3 * \sigma_{C-}}{| \mu_{C+} - \mu_{C-} |}$$

where σ_{C+} and σ_{C-} represent the standard deviations of the positive and negative control data, and μ_{C+} and μ_{C-} represent the means (Zhang *et al.*, 1999). The average Z′ score from the primary screen was 0.82, indicating a robust assay. CRCs were performed as described above but with varying concentrations of compound added.

Protein expression and purification

His_6-KIF15-N420, His_6-Eg5, and His_6-EGFP-HSET purifications have been described previously (Sturgill *et al.*, 2014, 2016; Dumas *et al.*, 2019). His_6-KIF15-N700 was expressed in High Five insect cells for 72 h, after which cells were pelleted and resuspended in lysis buffer (1× PNI [50 mM sodium phosphate, 500 mM NaCl, and 20 mM imidazole], 1% NP-40, 1 mM MgATP, 5 mM β-mercaptoethanol, and protease inhibitors (1 mM PMSF, 1 mM benzamidine, and LPC [10 μg/ml]) and incubated on ice for 30 min followed by sonication. Lysate was clarified by centrifugation for 30 min at 35,000 rpm at 4°C in a Type 45 Ti rotor (Beckman). Cleared lysate was incubated with 2 ml of Ni-NTA (nitrilotriacetic acid) agarose (Qiagen) for 1 h and washed with 50 ml of wash buffer (1× PNI, 100 μM MgATP, and 5 mM β-mercaptoethanol). Protein was eluted with elution buffer (1× PNI, 100 μM MgATP, 5 mM β-mercaptoethanol, and 200 mM imidazole), and peak fractions were combined and clarified by centrifugation for 5 min at 20,000 rpm at 4°C, after which they were subjected to size exclusion chromatography on a Superdex 200 column equilibrated in gel filtration buffer (10 mM K-HEPES [pH 7.7], 300 mM KCl, 1 mM DTT, and 0.2 mM MgATP). Protein concentration of fractions after gel filtration was estimated using a Bradford assay and purity of fractions was assessed by SDS–PAGE, after which peak fractions were combined and frozen with 10% sucrose.

Enzyme-coupled ATPase assay

KIF15-N420 ATPase rates were measured by quantifying the rate of NADH conversion in an enzyme-coupled reaction, as described by Huang *et al.* (Chen *et al.*, 2015; Huang *et al.*, 1994; Zaniewski *et al.*, 2020). The reaction contained BRB80 with 100 nM KIF15-N420 dimers, 2 mM phosphoenolpyruvate (Alfa Aesar, B20358), 1 mM MgCl2 (Quality Biological, 340-034-721), 0.2 mg/ml casein (Sigma, C-7078), 10 μM Taxol (Sigma, T7191), 0.25 mM NADH (EMD, 48915), and 1.5/100 vol of pyruvate kinase/lactate dehydrogenase (Sigma, P-0294). In the ATP-dependent assay, ATP concentration was varied and microtubule concentration held at 3 μM. In the microtubule-dependent assay, microtubule concentration was varied and ATP concentration was held at 2 mM. In each assay, 30 μM of the drug or an equal volume of DMSO for the control were included. Absorbance of NADH at 340 nm over time was measured on a Molecular Devices FlexStation 3 Multimode Microplate Reader, converted to an ATPase rate and divided by the active motor concentration to give the total hydrolysis cycle rate at 25°C.

The same enzyme-coupled reaction described for the ATPase assay was used to evaluate the IC_{50} for the compounds. This assay contained 2 mM ATP and 5 μM microtubules across all drug concentrations.

Microtubule gliding assays

Microtubule gliding assays were performed as previously described (Dumas *et al.*, 2019). Images were captured using a Nikon Elements controlled Eclipse 90i (Nikon) with a 100× 1.4 NA (Nikon) objective and a Cool Snap HQ2 charge-coupled device (CCD) camera (Roper). Time-lapse image sequences spanned 1 min with acquisitions captured every 5 s. ImageJ was used for image analysis, and gliding velocity was quantified by measuring the distance a microtubule traveled in 1 min. For each condition of each assay, image sequences were acquired from three locations on the slide and velocities were calculated from ≥15 microtubules in each location for a total of $n \geq 50$ from each slide.

For washout assays, image sequences were acquired for roughly 1 min predrug addition, 1 min postdrug addition, and 3 min postdrug washout for a total of 5 min captured. Gliding velocity for each time segment was quantified by measuring the distance a microtubule traveled over 1 min during each segment.

For analysis of microtubule binding, image sequences were captured before and after the addition of drug. The number of microtubules bound to the coverslip was quantified immediately before drug addition and after 1 min of drug incubation to calculate the percentage of microtubules that remained bound after drug addition.

Cell culture, immunofluorescence assays, and image analysis

TP53$^{-/-}$ RPE-1 and HeLa cells were cultured in DMEM containing 10% fetal bovine serum (FBS), penicillin, and streptomycin. RPE-1 KIRC-1 and HeLa KIRC-2 cells (Sturgill *et al.*, 2016) were cultured in the same medium with the addition of 10 μM STLC. For immunofluorescence assays, cells were grown on glass coverslips in 6-well dishes and then treated overnight with the desired drug concentrations added to their normal medium. Coverslips were rinsed with 1× phosphate-buffered saline (PBS) and fixed in 100% methanol at –20°C for 10 min and then stained with the following primary antibodies: rabbit anti-KIF15 (Sturgill and Ohi, 2013) at 1:2000 for 1 h and FITC–conjugated mouse anti-α-tubulin (DM1α, Sigma-Aldrich) at 1:500 for 30 min. Alexa-594–conjugated antirabbit secondary antibodies were used at 1:2000 for 45 min. All antibodies were incubated at RT. DNA was counterstained with 5 μg/ml Hoechst 33342 and coverslips were mounted in Prolong Diamond (Thermo Fisher Scientific).

Images were acquired using a 60× 1.4 NA objective (Olympus) on a DeltaVision Elite imaging system (GE Healthcare) equipped with a Cool SnapHQ2 CCD camera (Roper). Optical sections were

collected at 200-nM intervals and processed using the ratio deconvolution in SoftWorx (GE Healthcare). Further image processing and analysis was done in ImageJ. Acquisition parameters were kept constant across cell lines and conditions.

To quantify levels of KIF15 and tubulin on the mitotic spindle, an ROI was drawn around the spindle to measure the integrated fluorescence of a single image frame for both the KIF15 and tubulin channels. A smaller oval ROI was drawn outside of the spindle to measure background fluorescence on the KIF15 and tubulin channels. Background intensity corrected for ROI size was subtracted from the spindle intensity of each channel, and corrected intensities were used to calculate the KIF15:tubulin ratio.

Live cell imaging and analysis

TP53$^{-/-}$ RPE-1 cells were plated in MatTek dishes (Thermo Fisher Scientific) and grown to ~70% confluency. Desired compounds were diluted in Leibovitz's L-15 medium (Invitrogen) supplemented with 10% FBS and 7 mM K-HEPES, pH 7.7, and applied to cells. Time-lapse image sequences were captured using a 20× objective (Olympus) on the DeltaVision Elite imaging system using transmitted light microscopy. Optical sections were collected at 1.5-µm intervals every 2.5 min for 2–6 h.

Image sequences were analyzed in ImageJ to measure the time from metaphase plate formation to anaphase onset. Metaphase duration was quantified from 50 cells for each condition.

STLC selection

TP53$^{-/-}$ RPE-1 cells were plated in 6-well dishes and grown to ~80% confluency. Cells were then treated with the desired compounds added to DMEM medium supplemented with 10% FBS, penicillin, and streptomycin. Media were changed every 2–3 d for 24 d. At the endpoint, cells were rinsed with 1× PBS, fixed in 100% methanol at –20°C for 10 min, and stained with 0.1% crystal violet (Sigma Aldrich) in 25% methanol for 15 min at RT. Excess dye was removed by gentle washing with DI-H_2O. Images of dishes were acquired with a CanoScan 8800F (Cannon).

Compound synthesis methods

General techniques: all reactions requiring anhydrous conditions were conducted in flame-dried glass apparatus under an atmosphere of nitrogen. Preparative chromatographic separations were performed on silica gel (35–75 µm); reactions were followed by TLC analysis using silica plates with fluorescent indicator (254 nm) and visualized with a UV lamp or phosphomolybdic acid. All commercially available reagents were purchased from TCI or Aldrich and used as received unless stated otherwise. ^{1}H and ^{13}C NMR spectra were recorded in Fourier transform mode at the field strength specified on either a 500 or a 400 MHz spectrometer. Spectra were obtained in $CDCl_3$ or DMSO-d_6 solutions in 5-mm diameter tubes, and chemical shifts in ppm are quoted relative to the residual signal of chloroform (δH 7.26 ppm) or DMSO (δH 2.47). Multiplicities in the ^{1}H NMR spectra are described as s, singlet; d, doublet; t, triplet; q, quartet; m, multiplet; and br, broad; coupling constants are reported in Hz. Low (MS) and high (HRMS) resolution mass spectra are reported with ion mass/charge (*m/z*) ratios as values in atomic mass units.

Synthesis of 6-methyl-2-(methylthio)-6H-benzo[c] pyrimido[4,5-e][1,2]thiazine-8-carboxylic acid 5,5-dioxide (M-201)

Methyl 6-methyl-2-(methylthio)-6H-benzo[c]pyrimido[4,5-e][1,2]thiazine-8-carboxylate 5,5-dioxide 1 (Munesib-1) (100 mg, 0.28 mmol) was suspended in 4:1 DMF/H_2O (10 ml) followed by the addition of lithium hydroxide (34 mg, 1.4 mmol) in one portion. Dissolution eventually occurred and the solution was stirred at RT for overnight. The solution was diluted with 10 ml of H_2O and made acetic (pH = 1) with 2 M HCl. The precipitate was collected by filtration and washed with two portions of H_2O. The solid was then suspended in acetonitrile and filtered (2×). The filter cake was triturated with hexane and concentrated in vacuo to afford 68 mg (71%) of M-201 as a beige solid. HPLC: >98%, R_t = 6.23 min; ES-MS *m/z* 338.03 $[M+H]^+$; HNMR (DMSO-d_6, 400 MHz) 9.16 (s, 1H), 8.53 (d, J = 8 Hz, 1H), 7.95-7.86 (m, 2H), 3.15 (s, 3H), 2.68 (s, 3H) ppm.

Synthesis of (6-methyl-2-(methylthio)-5,5-dioxido-6H-benzo[c]pyrimido[4,5-e][1,2]thiazin-8-yl)(morpholino) methanone (M-202)

A mixture of M-201 (25 mg, 0.074 mmol) and 1-[Bis(dimethylamino) methylene]-1H-1,2,3-triazolo[4,5-b]pyridinium 3-oxide hexafluorophosphate (56 mg, 0.15 mmol) was treated with DMF (3 ml) followed by the addition of diisopropylethylamine (19 mg, 0.15 mmol). The solution was stirred at RT for 20 min at which time morpholine (14 mg, 0.16 mmol) was added. The solution was then stirred at 60°C for 2 h and evaluated by TLC (ethyl acetate): new product. The solution was stirred at 60°C for an additional 45 min, then cooled to RT and diluted with 10 ml H_2O and 25 ml of ethyl acetate. The organic phase was separated, washed with brine, dried (Na_2SO_4), and concentrated to an orange liquid. The liquid was taken up in dichloromethane and passed through a pad of silica gel eluting with ethyl acetate. Fractions containing the new product were combined and concentrated to afford M-202 as a yellow solid. Yield: 19 mg, 63%; HPLC: >95%, R_t = 6.06 min; HNMR ($CDCl_3$, 400 MHz) 9.0 (d, J = 0.6 Hz, 1H), 8.67 (d, J = 7.8 Hz, 1H), 7.39-7.28 (m, 2H), 3.82 (s, 4H), 3.66 (s, 2H), 3.53 (d, J = 0.7 Hz, 3H), 3.47 (s, 2H), 2.70 (d, J = 0.7 Hz, 3H) ppm; ES-MS *m/z* 407.08 $[M+H]^+$.

Synthesis of N,N-6-trimethyl-2-(methylthio)- 6H-benzo[c] pyrimido[4,5-e][1,2]thiazin-8-carboxamide 5,5-dioxide (M-203).

A mixture of M-201 (30 mg, 0.089 mmol) and 1-[Bis(dimethylamino) methylene]-1H-1,2,3-triazolo[4,5-b]pyridinium 3-oxide hexafluorophosphate (68 mg, 0.18 mmol) was treated with DMF (3 ml) followed by the addition of diisopropylethylamine (34 mg, 0.26 mmol). The solution was stirred at RT for 20 min at which time dimethylamine hydrochloride (46 mg, 0.56 mmol) was added. The solution was then stirred at 60°C for 2 h and evaluated by TLC (ethyl acetate): new product. The solution was stirred at 60°C for an additional 45 min, then cooled to RT and diluted with 10 ml H_2O and 25 ml of ethyl acetate. The organic phase was separated, washed with brine, dried (Na_2SO_4), and concentrated to an orange liquid. The liquid was taken up in dichloromethane and passed through a pad of silica gel eluting with ethyl acetate. Fractions containing the new product were combined and concentrated to a yield M-203 as a beige solid. The product was dried under high vacuum for 2 h. Yield: 25 mg, 77%; HNMR ($CDCl_3$, 400 MHz): 9.0 (s, 1H), 8.66 (dd, J = 7.9, 0.6Hz, 1H), 7.37 (dd, J = 9.3, 1.2 Hz, 2H), 3.53 (s, 3H), 3.16 (s, 3H), 3.02 (s, 3H), 2.7 (s, 3H) ppm; HPLC: 95%, R_t = 6.095 min; ES-MS *m/z* 365.07 $[M+H]^+$.

Synthesis of N- 6-dimethyl-2-(methylthio)-6H-benzo[c] pyrimido[4,5-e][1,2]thiazine-8-carboxamide 5,5-dioxide (M-204)

A mixture of M-201 (30 mg, 0.089 mmol) and 1-[Bis(dimethylamino) methylene]-1H-1,2,3-triazolo[4,5-b]pyridinium 3-oxide hexafluorophosphate (68 mg, 0.18 mmol) was treated with DMF (3 ml)

followed by the addition of diisopropylethylamine (34 mg, 0.26 mmol). The solution was stirred at RT for 20 min at which time methylamine hydrochloride (38 mg, 0.56 mmol) was added. The solution was then stirred at 60° C for 2 h and evaluated by TLC (ethyl acetate): new product. The solution was stirred at 60°C for an additional 45 min, then cooled to RT and diluted with 10 ml H_2O and 25 ml of ethyl acetate. The organic phase was separated, washed with brine, dried (Na_2SO_4), and concentrated to an orange liquid. The liquid was taken up in dichloromethane and passed through a pad of silica gel eluting with ethyl acetate. Fractions containing the new product were combined and concentrated to a yield M-204 as a yellow solid. The product was dried under high vacuum for 2 h. Yield: 13 mg, 42%; HNMR (DMSO-d_6, 400 MHz): 9.20 (s, 1H), 8.78 (d, J = 4.8 Hz, 1H), 8.61 (d, J = 8.3 Hz, 1H), 7.91 (d, J = 1.5Hz, 1H), 7.86 (dd, J = 8.2, 1.6 Hz, 1H), 3.49 (s, 3H), 2.83 (d, J = 4.5 Hz, 3H), 2.69 (s, 3H) ppm; HPLC: 90%, R_t = 5.99 min; ES-MS *m/z* 351.05 $[M+H]^+$

Synthesis of tert-butyl 4-(6-methyl-2-(methylthio)-5,5-dioxido-6H-benzo[c]pyrimido[4,5-e][1,2]thiazine-8-carbonyl) piperazine-1-carboxylate (I)

A mixture of M-201 (32 mg, 0.095 mmol) and 1-[Bis(dimethylamino) methylene]-1H-1,2,3-triazolo[4,5-b]pyridinium 3-oxide hexafluorophosphate (72 mg, 0.19 mmol) was treated with DMF (3.5 ml) followed by the addition of diisopropylethylamine (25 mg, 0.19 mmol). The solution was stirred at RT for 20 min at which time BOC-piperazine (39 mg, 0.21 mmol) was added. The solution was then stirred at 60°C for 2 h and evaluated by TLC (ethyl acetate): new product. The solution was stirred at 60°C for an additional 45 min, then cooled to RT and diluted with 10 ml H_2O and 25 ml of ethyl acetate. The organic phase was separated, washed with brine, dried (Na_2SO_4), and concentrated to a yellow liquid. The liquid was taken up in dichloromethane and passed through a pad of silica gel eluting with ethyl acetate. Fractions containing the new product were combined and concentrated to afford compound I (43 mg, 90%) as a yellow solid. HPLC: 95%, R_t = 7.23 min.

Synthesis of (6-methyl-2-(methylthio)-5,5-dioxido-6H-benzo[c]pyrimido[4,5-e][1,2]thiazin-8-yl)(piperazin-1-yl) methanone (M-205)

The BOC-protected piperazine derivative I (29.5 mg, 0.058 mmol) was taken up in 4 ml of dichloromethane followed by the dropwise addition of trifluoroacetic acid (0.4 ml). The solution was stirred at RT for overnight, then diluted with 30 ml of dichloromethane and washed with 12 ml of 10% sodium carbonate, brine, and dried over Na_2SO_4. The solvent was concentrated in vacuo affording M-205 (23 mg, 97%) as a yellow solid. HPLC: 95%, R_t = 4.94 min;HNMR ($CDCl_3$, 400 MHz) 9.0 (s, 1H), 8.66 (d, J = 8.3Hz, 1H), 7.34 (td, J = 4.2, 1.5Hz, 2H), 3.80 (s, 2H), 3.53 (s, 3H), 3.41 (s, 2H), 2.99 (s, 2H), 2.84 (s, 2H), 2.70 (s, 3H), 1.25 (s, 1H) ppm; ES-MS *m/z* 406.09 $[M+H]^+$.

Synthesis of 8-(hydroxymethyl)-6-methyl-2-(methylthio)-6H-benzo[c]pyrimido[4,5-e][1,2]thiazine 5,5-dioxide (M-206)

M-201 (30 mg, 0.089 mmol) was suspended in dichloromethane (5 ml) followed by the addition of oxalyl chloride (41 mg, 0.32 mmol) and one drop of DMF. The mixture became a solution after stirring at RT for 30 min. The solution was stirred for an additional 30 min at which time it was concentrated in vacuo. The solid obtained (32 mg, 100%) was used in the next step without further purification. The crude acid chloride (32 mg, 0.090 mmol) was taken up in 4 ml of tetrahydrofuran and cooled in an ice bath to approximately 0°C. To the solution lithium aluminum hydride was added in several portionsz (10 mg, 0.27 mmol). The mixture was gradually warmed to RT and was quenched with sat. aq. $NaHPO_4$. The mixture was diluted with ethyl acetate and filtered through celite. The filtrate was washed with brine, dried ($MgSO_4$), and concentrated to a solid. The crude product was passed through a pad of silica gel eluting with 9:1 dichloromethane/ethyl acetate. Fractions containing the product were combined and concentrated to give M-206 as a yellow solid (9 mg, 30%). HNMR ($CDCl_3$, 400 MHz): 8.97 (s, 1H), 8.59 (d, J = 8.1Hz, 1H), 7.39-7.29 (m, 2H), 4.87 (d, J = 5.2Hz, 2H), 3.52, s, 3H), 2.70 (s, 3H), 1.95 (t, J = 5.9Hz, 1H) ppm; HPLC: 99%, R_t = 5.96 min; ES-MS *m/z* 324.047 $[M+H]^+$.

ACKNOWLEDGMENTS

We thank the Ohi lab that made this work possible, as well as Emma Sturgill, Megan Dumas, and George Xu for doing extensive optimization of these assays. We thank Steve Vander-Roest and Andrew Alt from the Center for Chemical Genomics and Peter Toogood and Pil Lee from Michigan Drug Discovery for all of their invaluable effort, expertise, and advice on screening methods and medicinal chemistry. This work was supported by National Institutes of Health (NIH) Grant R01 GM086610, pilot project funding from Michigan Drug Discovery Grant MDD2019204-RCC, funding from the University of Michigan Rogel Cancer Center, start-up funds from the University of Michigan, and NIH Grant R35 GM139568 to W.O.H.

REFERENCES

Bakhoum SF, Genovese G, Compton DA (2009). Deviant kinetochore–microtubule dynamics underlie chromosomal instability. Curr Biol 19, 1937–1942.

Begley MA, Solon AL, Davis EM, Sherrill MG, Ohi R, Elting MW (2021). K-fiber bundles in the mitotic spindle are mechanically reinforced by Kif15. Mol Biol Cell 32, br11.

Chen GY, Arginteanu DFJ, Hancock WO (2015). Processivity of the Kinesin-2 KIF3A results from rear head gating and not front head gating. J Biol Chem 290, 10274–10294.

Cohen-Sharir Y, McFarland JM, Abdusamad M, Marquis C, Bernhard SV, Kazachkova M, Tang H, Ippolito MR, Laue K, Zerbib J, *et al.* (2021). Aneuploidy renders cancer cells vulnerable to mitotic checkpoint inhibition. Nature 590, 486–491.

DeBonis S, Skoufias DA, Lebeau L, Lopez R, Robin G, Margolis RL, Wade RH, Kozielski F (2004). In vitro screening for inhibitors of the human mitotic kinesin Eg5 with antimitotic and antitumor activities. Mol Cancer Ther 3, 1079–1090.

Dumas ME, Chen G-Y, Kendrick ND, Xu G, Larsen SD, Jana S, Waterson AG, Bauer JA, Hancock W, Sulikowski GA, Ohi R (2019). Dual inhibition of Kif15 by oxindole and quinazolinedione chemical probes. Bioorg Med Chem Lett 29, 148–154.

Elkins JM, Fedele V, Szklarz M, Abdul Azeez KR, Salah E, Mikolajczyk J, Romanov S, Sepetov N, Huang XP, Roth BL, *et al.* (2016). Comprehensive characterization of the published kinase inhibitor set. Nat Biotechnol 34, 95–103.

Gampa G, Kenchappa RS, Mohammad AS, Parrish KE, Kim M, Crish JF, Luu A, West R, Hinojosa AQ, Sarkaria JN, *et al.* (2020). Enhancing brain retention of a KIF11 inhibitor significantly improves its efficacy in a mouse model of glioblastoma. Sci Rep 10, 1–13.

Gascoigne KE, Taylor SS (2009). How do anti-mitotic drugs kill cancer cells? J Cell Sci 122, 2579–2585.

Gayek AS, Ohi R, Bloom KS (2014). Kinetochore–microtubule stability governs the metaphase requirement for Eg5. MBoC 25.

Hentrich C, Surrey T (2010). Microtubule organization by the antagonistic mitotic motors kinesin-5 and kinesin-14. J Cell Biol 189, 465–480.

Huang TG, Suhan J, Hackney DD (1994). Drosophila kinesin motor domain extending to amino acid position 392 is dimeric when expressed in Escherichia coli. J Biol Chem 269, 16502–16507.

Kapitein LC, Peterman EJG, Kwok BH, Kim JH, Kapoor TM, Schmidt CF (2005). The bipolar mitotic kinesin Eg5 moves on both microtubules that it crosslinks. Nature 435, 114–118.

Kapoor TM, Mayer TU, Coughlin ML, Mitchison TJ (2000). Probing spindle assembly mechanisms with monastrol, a small molecule inhibitor of the mitotic kinesin, Eg5 7. J Cell Biol 150, 975–988.

Kasap C, Elemento O, Kapoor TM (2014). DrugTargetSeqR: A genomics- and CRISPR-Cas9-based method to analyze drug targets. Nat Chem Biol 10, 626–628.
Kashina AS, Baskin RJ, Cole DG, Wedaman KP, Saxton WM, Scholey JM (1996). A bipolar kinesin. Nature 379, 270–272.
Khodjakov A, Copenagle L, Gordon MB, Compton DA, Kapoor TM (2003). Minus-end capture of preformed kinetochore fibers contributes to spindle morphogenesis. J Cell Biol 160, 671–683.
Komlodi-Pasztor E, Sackett DL, Wilkerson J, Fojo T (2011). Mitosis is not a key target of microtubule agents in patient tumors. Nat Rev Clin Oncol 8, 244–250.
Lampson MA, Renduchitala K, Khodjakov A, Kapoor TM (2004). Correcting improper chromosomes-spindle attachments during cell division. Nat Cell Biol 6, 232–237.
Maiato H, Rieder CL, Khodjakov A (2004). Kinetochore-driven formation of kinetochore fibers contributes to spindle assembly during animal mitosis. J Cell Biol 167, 831–840.
Mann BJ, Wadsworth P (2019). Kinesin-5 Regulation and Function in Mitosis. Trends Cell Biol 29, 66–79.
Mardin BR, Isokane M, Cosenza MR, Krämer A, Ellenberg J, Fry AM, Schiebel E (2013). EGF-induced centrosome separation promotes mitotic progression and cell survival. Dev Cell 25, 229–240.
Marquis C, Fonseca CL, Queen KA, Wood L, Vandal SE, Malaby HLH, Clayton JE, Stumpff J (2021). Chromosomally unstable tumor cells specifically require KIF18A for proliferation. Nat Commun 12, 1213.
Marzo I, Naval J (2013). Antimitotic drugs in cancer chemotherapy: Promises and pitfalls. Biochem Pharmacol 86, 703–710.
Mayer TU, Kapoor TM, Haggarty SJ, King RW, Schreiber SL, Mitchison TJ (1999). Small molecule inhibitor of mitotic spindle bipolarity identified in a phenotype-based screen. Science 286, 971–974.
Milic B, Chakraborty A, Han K, Bassik MC, Block SM (2018). KIF15 nanomechanics and kinesin inhibitors, with implications for cancer chemotherapeutics. Proc Natl Acad Sci USA 115, E4613–E4622.
Mitchison TJ, Maddox P, Gaetz J, Groen A, Shirasu M, Desai A, Salmon ED, Kapoor TM (2005). Roles of polymerization dynamics, opposed motors, and a tensile element in governing the length of Xenopus extract meiotic spindles. Mol Biol Cell 16, 3064–3076.
Mountain V, Simerly C, Howard L, Ando A, Schatten G, Compton DA (1999). The kinesin-related protein, Hset, opposes the activity of Eg5 and cross-links microtubules in the mammalian mitotic spindle. J Cell Biol 147, 351–366.
Oriola D, Needleman DJ, Brugués J (2018). The physics of the metaphase spindle. Annu Rev Biophys 47, 655–673.
Quinton RJ, DiDomizio A, Vittoria MA, Kotýnková K, Ticas CJ, Patel S, Koga Y, Vakhshoorzadeh J, Hermance N, Kuroda TS, *et al.* (2021). Whole genome doubling confers unique genetic vulnerabilities on tumor cells. Nature 590, 492–497.
Raaijmakers JA, van Heesbeen RGHP, Meaders JL, Geers EF, Fernandez-Garcia B, Medema RH, Tanenbaum ME (2012). Nuclear envelope-associated dynein drives prophase centrosome separation and enables Eg5-independent bipolar spindle formation. EMBO J 31, 4179–4190.
Sturgill EG, Ohi R (2013). Kinesin-12 differentially affects spindle assembly depending on its microtubule substrate. Curr Biol 23, 1280–1290.
Sturgill EG, Das DK, Takizawa Y, Shin Y, Collier SE, Ohi MD, Hwang W, Lang MJ, Ohi R (2014). Kinesin-12 kif15 targets kinetochore fibers through an intrinsic two-step mechanism. Curr Biol 24, 2307–2313.
Sturgill EG, Norris SR, Guo Y, Ohi R (2016). Kinesin-5 inhibitor resistance is driven by kinesin-12. J Cell Biol 213, 213–227.
Tanenbaum ME, Macůrek L, Janssen A, Geers EF, Alvarez-Fernández M, Medema RH (2009). Kif15 cooperates with Eg5 to promote bipolar spindle assembly. Curr Biol 19, 1703–1711.
Vanneste D, Takagi M, Imamoto N, Vernos I (2009). The role of Hklp2 in the stabilization and maintenance of spindle bipolarity. Curr Biol 19, 1712–1717.
Wilson JE (2003). Isozymes of mammalian hexokinase: Structure, subcellular localization and metabolic function. J Exp Biol 206, 2049–2057.
Zaniewski TM, Gicking AM, Fricks J, Hancock WO (2020). A kinetic dissection of the fast and superprocessive kinesin-3 KIF1A reveals a predominant one-head-bound state during its chemomechanical cycle. J Biol Chem 295, 17889–17903.
Zhang JH, Chung TDY, Oldenburg KR (1999). A simple statistical parameter for use in evaluation and validation of high throughput screening assays. J Biomol Screen 4, 67–73.